Asia-Pacific Journal of Atmospheric Sciences (2022) 58:415–433
https://doi.org/10.1007/s13143-021-00262-1

Online ISSN 1976-7951
Print ISSN 1976-7633

ORIGINAL ARTICLE

Asymmetric Structures of a Squall-Line MCS over Taiwan with Significant Hydraulic Jumps

Yu-Tai Pan[1] · **Ming-Jen Yang**[1]

Received: 15 March 2021 / Revised: 12 July 2021 / Accepted: 20 September 2021 / Published online: 22 October 2021

Abstract

On 19 April 2019, a mature squall-line mesoscale convective system (MCS) with the characteristics of a leading convective line and trailing stratiform landed on Taiwan, resulting in strong gust wind and heavy rainfall. This squall-line MCS became asymmetric after landfall on Taiwan. Two sets of idealized numerical simulations (mountain heights and low-level vertical wind shear) using the Weather Research and Forecasting (WRF) model were conducted to examine the impacts of realistic Taiwan topography on a squall-line MCS. Results showed numerous similarities between the idealized simulations and real-case observations. The low-level Froude number which considered the terrain height (F_{mt}) was calculated to examine the blocking effect of the Taiwan terrain, and the cold pool (determined by − 1.5 K isotherm) was found to be completely blocked by the 500-m height contour. The northeast-southwest orientation of the Snow Mountain Range (SMR), and the north–south orientation of the Central Mountain Range (CMR) led to the upwind side asymmetry. On the other hand, the lee-side asymmetry was associated with different intensities and occurrence locations of the hydraulic jump between the SMR and southern CMR, and the cold-pool Froude number (F_{cp}) indicated the flow-regime transition from subcritical to supercritical.

Keywords Squall-line MCS · Taiwan topography · Froude number · Hydraulic jump

1 Introduction

During the Mei-Yu season (from mid-May to mid-June) in Taiwan, the squall-line type of mesoscale convective systems (MCSs) frequently form ahead of or along the Mei-Yu fronts over southeastern China, which approach Taiwan from the west and lead to heavy rainfall and fierce gust wind (Fang 1985; Ninomiya et al. 1988). Ahead of the squall line, the environment usually has substantial vertical wind shear (particularly at low level), and the interaction between environmental wind shear and precipitation-induced cold pool can make the squall-line MCS a self-organized system (Fovell and Tan 1998; Lin et al. 1998; Lin and Joyce 2001).

There are relatively few studies on the terrain effects to squall-line MCSs. Since Taiwan is a mountainous island, the relation between a squall-line MCS and realistic Taiwan terrain is worth investigating. One previous observational study (Teng et al. 2000) investigated the impacts of Taiwan terrain on a squall-line MCS during the Taiwan Area Mesoscale experiment (TAMEX; Kuo and Chen 1990), and they found the orientation of squall-line MCS became parallel to 1000-m terrain contour line after the contacts with Taiwan topography.

The evolution of a squall-line MCS is strongly determined by cold-pool dynamics. Cold pool is a region with substantial evaporative cooling produced by precipitation, a key feature to initiate new convective cells at the leading edge and sustain the MCS (Rotunno et al 1988; Weisman 1993; Yang and Houze 1995a, b; Weisman and Rotunno 2004). As a result, whether the cold pool is blocked by terrain or not affects the longevity of the squall-line MCS (Frame and Markowski 2006; Letkewicz and Parker 2011).

After the contact with the terrain, the squall-line MCS would either dissipate away or reinitiate convection on the lee side, depending on the hydraulic jump effect (Long

Communicated by Hyeyum Hailey Shin

✉ Ming-Jen Yang
mingjen@as.ntu.edu.tw

[1] Department of Atmospheric Sciences, National Taiwan University, No. 1, Sec. 4, Roosevelt Road, Taipei 10617, Taiwan

1953). Numerous modeling studies examined the relation between the downslope motion and hydraulic jump effect on the lee side (Durran 1986, 1990; Karyampudi et al. 1995; Frame and Markowski 2006; Armi and Mayr 2011). The hydraulic jump occurs when the flow makes a transition from subcritical flow upstream to supercritical flow over the mountain, and the Froude number which considered cold pool depth (F_{cp}) is utilized to decide whether the fluid is supercritical ($F_{cp} > 1$) or subcritical ($F_{cp} < 1$).

The objectives of this study are listed as follows. Firstly, we use the mountain-height Froude number (F_{mt}) to clarify the asymmetric structure on the upwind side and the cold-pool blocking effect due to Taiwan terrain. Secondly, the cold-pool Froude number (F_{cp}) is applied to discuss the leeside asymmetry. The transition from subcritical flow ($F_{cp} < 1$) upstream to supercritical flow ($F_{cp} > 1$) at mountain peak favors the hydraulic jump effect, which can reinitiate convection on lee side. Lastly, the terrain-heights and low-level shear experiments are conducted to further examine the control simulation results.

Previous studies mainly applied a bell-shaped mountain in idealized simulations to discuss the impacts of the terrain on squall-line MCS (Frame and Markowski 2006; Reeves and Lin 2007; Letkewicz and Parker 2011), which may not be suitable for the complicated terrain on Taiwan. Hence, instead of using an idealized terrain, idealized WRF simulations with realistic Taiwan topography are conducted to examine the influences of complex Taiwan topography on a squall line. The mature squall-line MCS case with a symmetric precipitation structure which landed over Taiwan on 19 April 2019 is a case for us to compare with the results obtained from the idealized simulations.

This paper is organized as follows. Overview of the sqaull-line MCS event on 19 April 2019 is in Sect. 2. Methodology is presented in Sect. 3. Results from idealized model simulations are discussed in Sect. 4. The conclusions are summarized in Sect. 5.

2 Case Overview

On 19 April 2019, a mature squall-line MCS formed over southeastern China and moved eastward to Taiwan, developing its mature stage and remained symmetric before being affected by Taiwan terrain. Figure 1 illustrates the radar reflectivity evolution of this squall-line system. Before

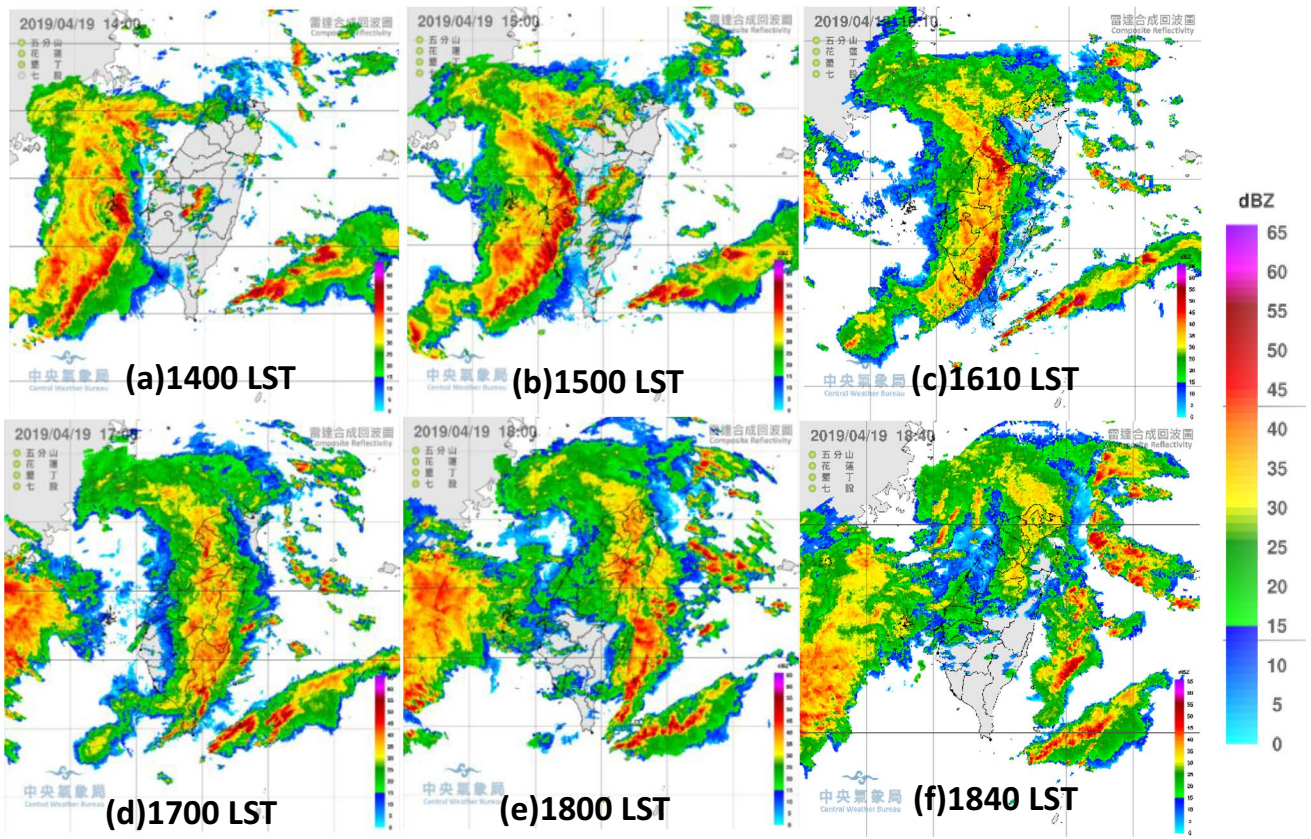

Fig. 1 Composite of vertical-maximum (CV) radar reflectivity (in units of dBZ) maps on 19 April 2019: **a** 1400 LST, **b** 1500 LST, **c** 1610 LST, **d** 1700 LST, **e** 1800 LST, and **f** 1840 LST (Image source: Central Weather Bureau in Taiwan)

reaching Taiwan, the precipitation feature of this squall line was mostly symmetric (Fig. 1a). Even when the squall line just touched Taiwan's coast line, the precipitation structure did not alter significantly (Fig. 1b).

After landing on Taiwan's mountainous area, this squall line changed its structure. It is clear from Fig. 1c that the orientation of the southern leading line became roughly north–south orientation, but the northern leading line remained the same northwest-southeast orientation as previous stage (Fig. 1b). The southern part of the squall line also showed slightly stronger radar echoes than the northern counterpart (Fig. 1c, d). It is clear that the variation of the squall-line orientation resulted from the impacts by Taiwan terrain. The different leading line orientation on the upwind side of the mountain is called "upwind side asymmetry". Later, the squall line moved to the lee side of the mountain (Fig. 1e). Notice that the southern part of the squall line moved faster than the northern part, and this asymmetry is called "leeside asymmetry". Finally, the squall-line system progressed to the east of Taiwan and dissipated eventually (Fig. 1f).

3 Methodology

3.1 Model Design

The Advanced Research version of the Weather Research and Forecasting model (WRF-ARW version 3.9; Skamarock et al. 2008) was used to perform the idealized simulations in this study. In a real-case WRF simulation, synoptic forcing, Coriolis force, radiation, and topography are all included, and these physical processes will all affect the symmetry of a squall-line MCS, causing us difficult to isolate the terrain effects on a squall line. As a result, we used the idealized WRF simulation to exclusively investigate the terrain impacts on a squall-line MCS.

The computational domain was 1400 km in the x direction and 940 km in the y direction with a horizontal grid size of 2 km. Since a mature squall line can develop vertically up to 15 km in vertical, we set the domain vertical top to be 30 km with 55 stretched vertical levels. A sponge layer with a damping coefficient of 0.0003 s^{-2} was applied to the top 5 km to prevent energy reflection from the upper boundary. The open condition was imposed for the lateral boundaries, and the time step was 3 s.

The physical parameterization schemes used in the model include the WDM6 microphysics parameterization (Lim and Hong 2010) and the Yonsei University (YSU) planetary boundary layer (PBL) parameterization (Hong and Pan 1996). Weisman et al. (1997) indicated that resolutions of 4 km might be sufficient to reproduce much of the mesoscale structure and evolution of the squall line-type convective systems produced in 1-km simulations. Thus, a horizontal grid size of 2 km is used in this study, based on the compromise between the limitation of available computational resources, numbers of numerical experiments, and the grid resolution required to resolve deep convective cells. The cumulus parameterization is not used. Effects of Coriolis force and radiation are ignored in this study in order to emphasize the effects of Taiwan terrain.

For the environmental setting, instead of using the observed sounding directly, we alternatively use a composite sounding. The reason is that we only have the observed sounding data at 00 UTC (08 LST) and 12 UTC (20 LST), but the squall-line MCS case occurred from 13 to 18 LST (see Fig. 1); as a result, both the 00 UTC and 12 UTC data cannot be used to fully determine the environmental condition before the arrival of MCS. In fact, the 00 UTC sounding in either Makong (a small island west of Taiwan; see its location in Fig. 3) or Panchiao (northern Taiwan; also shown in (Fig. 3) contained convective available potential energy (CAPE) of less than 200 J kg^{-1} which did not favor squall-line initiation in an idealized model setting. This low-CAPE situation might result from earlier convective precipitation occurring before the arrival of this squall line and the contribution from sea breeze from the surrounding ocean.

The pre-storm environment is horizontally homogeneous in the idealized model setting. A composite sounding with a surface temperature of 301.5 K (28.5 °C) and a surface mixing ratio of water vapor of 21.3 g kg^{-1} is given, and this environment contains the CAPE of 2588 J kg^{-1} (Fig. 2a). This thermodynamic sounding is a composite from several sounding stations in Taiwan with high CAPEs during the Southwest Monsoon Experiment field project (SoWMEX; Jou et al. 2011) to represent the environmental characteristic of Mei-Yu season. Although the SoWMEX campaign was conducted more than 10 years ago, it is still the most recent field experiment which had the most complete intense observations (including surface, sounding, radar, satellite, and aircraft measurements) in Taiwan during the Mei-Yu season. Therefore, a composite sounding from SoWMEX can still show the representative theromydnamic profile in Taiwan during the Mei-Yu season.

The observed wind profile at Makong (Fig. 2b) showed that there was strong vertical shear at low levels (0–2.5 km). Recall that the squall-line longevity is most sensitive to the low-level (0–3 km AGL) vertical wind shear perpendicular to squall-line orientation (Rotunno et al. 1988; Weisman and Rotunno 2004); as a result, we ignore the wind variations at middle to upper levels at Makong for simplification. Thus, we only consider the horizontal wind perpendicular to the squall line, namely, the zonal wind. The wind speed increases linearly from zero at the surface to 10 m s^{-1} at the altitude of 2500 m (based on the observed wind profile in

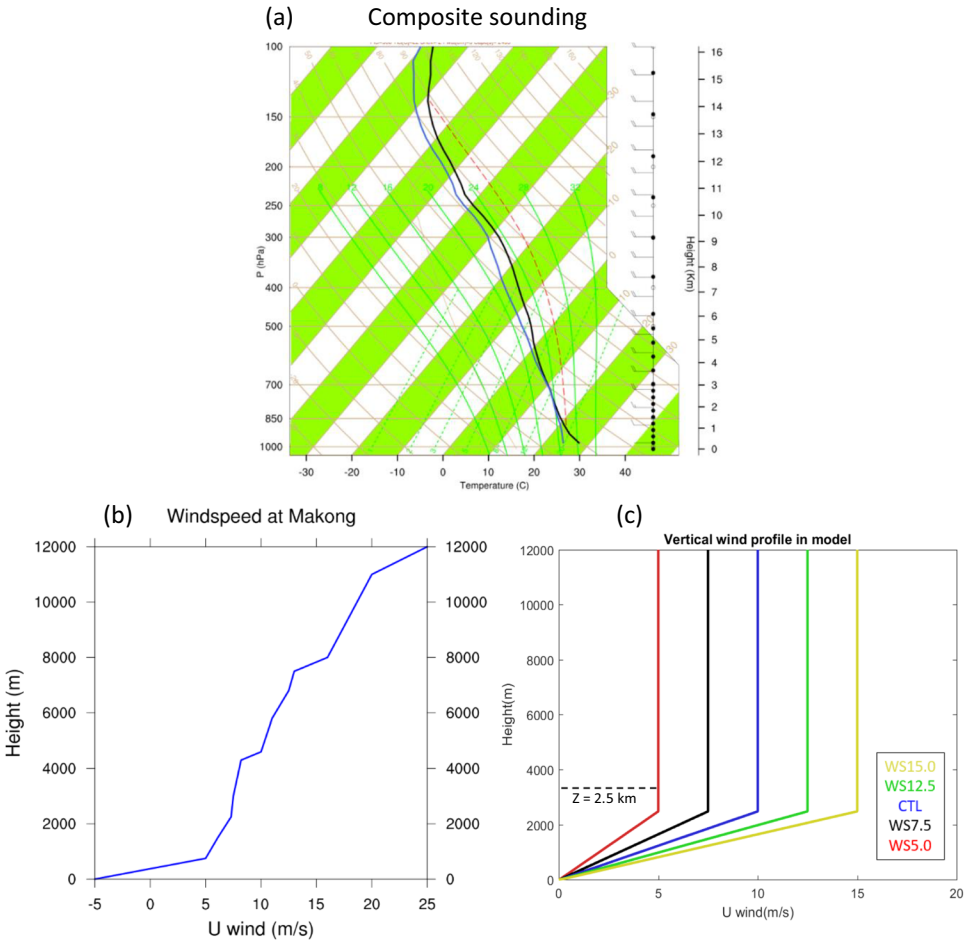

Fig. 2 **a** Composite sounding adapted from soundings in the SoWMEX field project. The surface temperature is 28.5 °C and the mixing ratio of water vapor is 23.3 g Kg^{-1} near the surface. Black and blue lines represent temperature and dew-point temperature. **b** Observed zonal wind profile at Makong at 00 UTC 19 April 2019. **c** Zonal wind profiles in low-level wind-shear experiments. The wind-shear below 2.5-km height is 5, 7.5, 10.0, 12.5, and 15.0 m s^{-1}, respectively

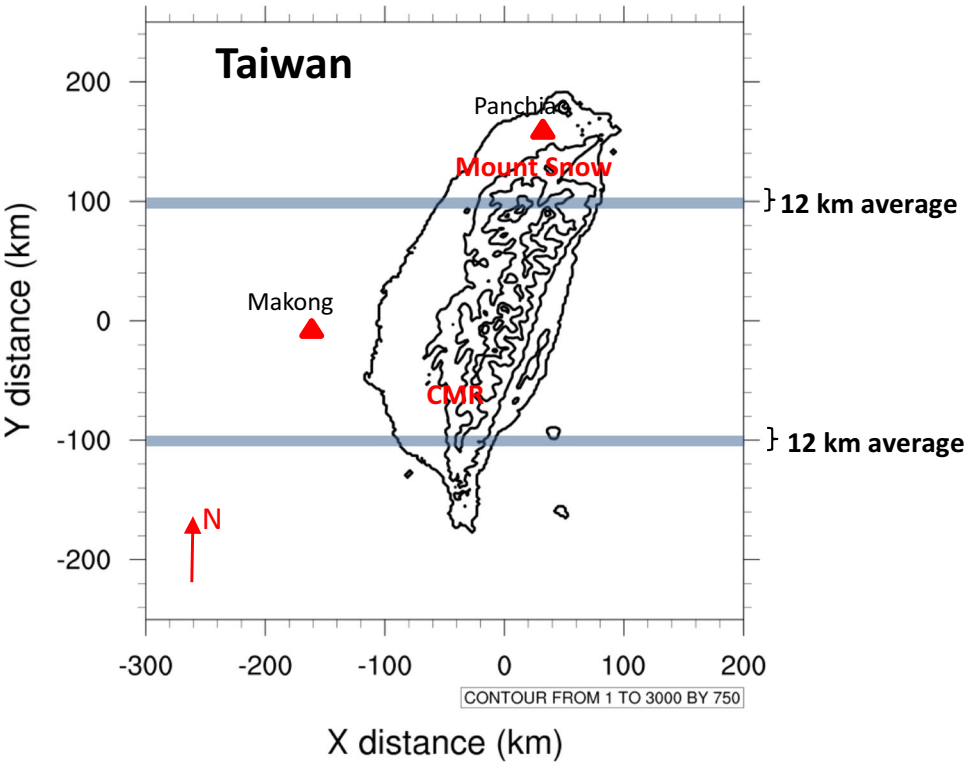

Fig. 3 Realistic Taiwan terrain after 9-point moving average. The Taiwan topography is located at the center of the computational domain. Terrain heights are contoured at 1, 500, 1500, 2500 and 3000 m, respectively. The upper (lower) blue line is the horizontal position for the 12-km averaged vertical cross section in Fig. 11 (12), and the red triangles indicate the locations of Panchiao and Makong

Makong), and the wind velocity is assumed to be constant above 2500 m (Fig. 2c).

3.2 Experiment Design

Most of previous studies (Frame and Markowski 2006; Reeves and Lin 2007; Letkewicz and Parker 2011) used a bell-shaped topography to discuss the relation between terrain and squall-line MCS, but the idealized terrain is too simplified to represent the complicated topography like Taiwan. Since we plan to understand impacts of Taiwan terrain on squall-line MCS, the realistic Taiwan topography is necessary. Therefore, a high-resolution (30 m) Taiwan topography data was used. We downscaled the raw topography data to the model grid with 2-km horizontal grid size, and located the Taiwan terrain at the center of computational domain. Additionally, a 9-point moving average was performed to smooth the terrain to avoid numerical instability in the WRF model. The highest terrain peak is 3312 m and the main characteristic of Taiwan topography is captured (Fig. 3), including Mount Snow and the Central Mountain Range (CMR).

A long warm bubble was used to initiate the squall-line convection, and the lee side gravity-wave convection was produced by the westerly flow over the Taiwan terrain (Fig. 4). This lee-side convection phenomenon is common when the prevailing wind flowed over topography (Chu and Lin 2000; Chen and Lin 2005; Reeves and Lin 2007; Miglietta and Rotunno 2009). In order to reduce the influence of the lee side convection and precipitation on the squall-line MCS, the line-type warm bubble was put into the model sometime after the initialization. After trial and error, we found that a warm bubble of 4 K, with the size of 200 km in length (north–south), 25 km in width (east–west) and 1.5 km deep, added at the quarter of the x direction and half of the y direction at model time of 4 h, can have minimal impacts of lee-side convection and precipitation. The size of the initial thermal was chosen to mimic the observed squall-line characteristics shown in Fig. 1a.

3.3 Froude Numbers Used in This Study

Two definitions of Froude number are used in this study. One is the Froude number considering mountain height (F_{mt}), and the other is Froude number considering the cold-pool depth (F_{cp}). The details are discussed as follows.

Froude number which considers the mountain height (F_{mt}) is a useful non-dimensional parameter when we discuss the flow impinging on the steep mountains and the blocking effect. Mechanically, whether the flow contains enough kinetic energy to overcome potential energy of the terrain barrier (Reeves and Lin 2007) can be determined by F_{mt}, which is defined as

$$F_{mt} = \frac{U_{avg}}{N_{avg} \times H_{mt}}, \tag{1}$$

$$N = \sqrt{\frac{g}{\theta_v} \times \frac{d\theta_v}{dz}}, \tag{2}$$

where U_{avg} is the averaged wind speed for air within the atmospheric volume below 1 km shown in Fig. 20, N_{avg} is the averaged Brunt–Väisälä frequency (s^{-1}) within the same

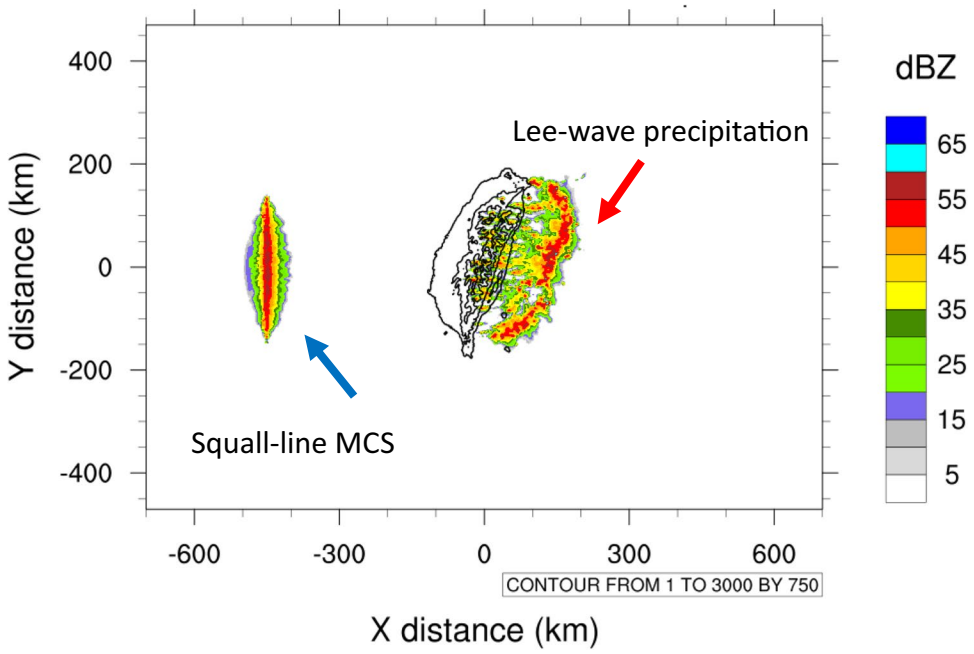

Fig. 4 Simulated radar reflectivity CV plot at 5 h of model simulation. Red arrow denotes the lee-wave convection discussed in the text, and blue arrow denotes the embryo squall-line MCS initiated by the line-type warm thermal

atmospheric volume, H_{mt} is mountain peak height (m), g is gravitational acceleration (m s^{-2}) and θ_v is virtual potential temperature (K). Please see Appendix for the detailed procedure of calculating F_{mt}.

If F_{mt} is greater than 1, low-level air flow can climb over the mountain; on the other hand, if F_{mt} is less than 1, low-level airflow will turn around the mountain and converge on the lee side. To understand the blocking effect on air flow near Taiwan terrain, we choose a specific location and timing to calculate the F_{mt} as shown in Fig. 5. The timing and space are chosen when the simulated squall-line MCS just lands on Taiwan.

For the Froude number which considers the cold-pool depth (F_{cp}), the formula is similar as F_{mt} except for H_{cp} term, which follows that in Frame and Markowski (2006)

$$F_{cp} = \frac{U}{N \times H_{cp}}, \tag{3}$$

$$N = \sqrt{\frac{g}{\theta_v} \times \frac{d\theta_v}{dz}}, \tag{4}$$

where U is the wind speed, N is Brunt-Väisälä frequency, H_{cp} is cold-pool depth (assumed to be 1.5 km), g is gravitational acceleration (m s^{-2}) and θ_v is virtual potential temperature (K). Please see Appendix for the procedure of calculating F_{cp}.

The F_{cp} is used to identify whether the flow regime is subcritical ($F_{cp} < 1$) or supercritical ($F_{cp} > 1$). As mentioned in the introduction, the hydraulic jump helps to reinitiate convection on the lee side, and it occurs when the flow makes a transition from subcritical at upstream to supercritical at mountain peak (Durran 1986, 1990).

3.4 Spatial Correlation Coefficient

In our numerical experiments, the symmetry of a squall-line MCS is not easy to determine visually; thus, in order to objectively quantify the degree of symmetry of a squall line, a spatial correlation coefficient (SCC) is utilized (Tai et al. 2017). The SCC is defined as

$$SCC = \frac{\sum \left(x_n - \overline{x_n}\right)\left(x_s - \overline{x_s}\right)}{\sqrt{\left(\Sigma\left(x_n - \overline{x_n}\right)^2 \Sigma\left(x_s - \overline{x_s}\right)^2\right.}}, \tag{5}$$

where variable x denotes the value of radar reflectivity, subscript n and s denote the north and south parts of the squall-line MCS respectively, and the overbar ($\bar{}$) is the average over either the northern or southern region.

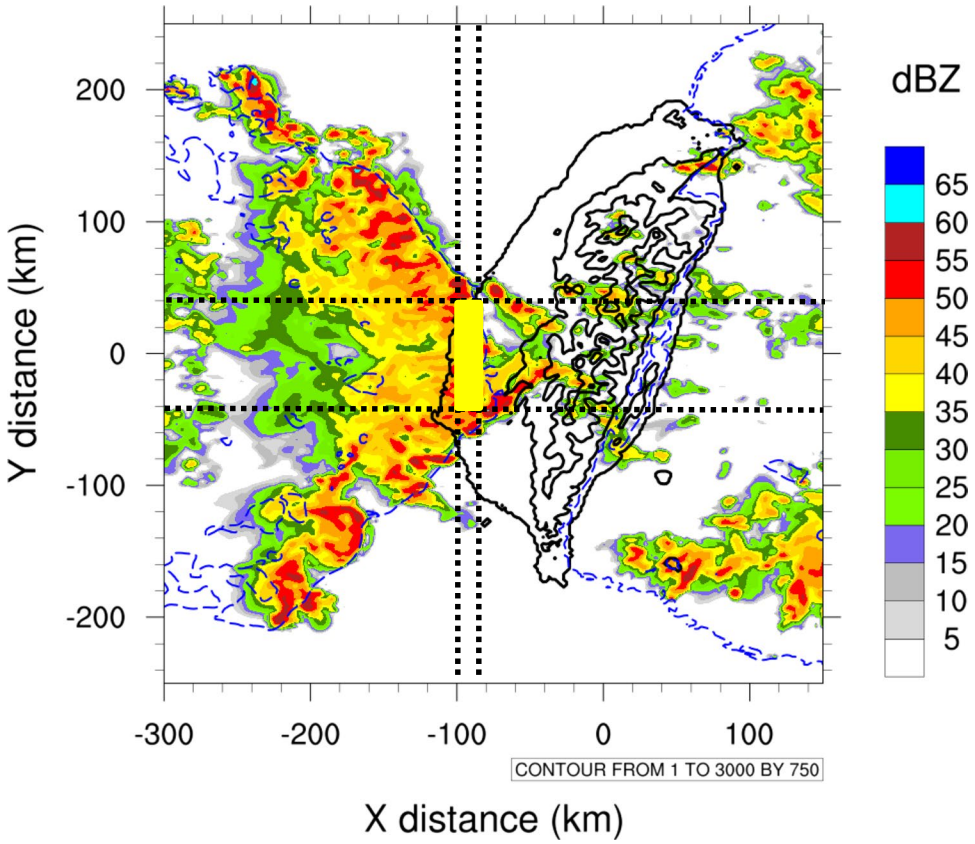

Fig. 5 The spatial range chosen for calculating the mountain-height Froude number (F_{mt}). The time and space are chosen when the squall-line MCS just lands on Taiwan. The spatial range of the yellow region is: $x = -90 \sim -100$ km, $y = -40 \sim +40$ km, $z = 1$ km above the surface

Figure 6 shows the calculation procedure. Firstly, we designate the leading edge of the squall-line MCS as the rightmost boundary of the given rectangle. Secondly, the central line is defined as the line ($y=0$) to divide a symmetric squall line into the northern part and the southern counterpart, and the rectangle area in both parts are 200 km in length and 120 km in width. Notice that we ignore the missing-value region (the default radar reflectivity is − 30 dBZ) to avoid the overestimation of the SCC. Therefore, the structure of a squall line is more symmetric as the SCC is closer to 1. People might argue whether the central line ($y=0$) we chose is fair or not, because the rightmost leading edge may not be always at the central line ($y=0$). Thus, additional central-line uncertainty experiments are also conducted. We adjust the central-line position either 5 km north or south from $y=0$ to represent the position uncertainty, and results indicate that the SCC percentage error is less than 5% (not shown). Hence, regarding the axis at $y=0$ as the central line to divide the squall-line system into the northern and southern part should be reasonable.

3.5 Sensitivity Experiments

In addition to the control experiment, two sets of sensitivity experiments are done. When we consider the impacts of Taiwan terrain on a squall-line MCS, Froude number F_{mt} is a critical parameter which is dynamically controlled by the mountain peak height and the zonal wind. As a result, both the terrain-height (Table 1) and low-level wind-shear (Table 2) sensitivity experiments are performed to investigate the relation between Froude number (F_{mt}) and the structure of squall-line MCS. Note that for the no-terrain experiment (NTR), the whole island of Taiwan was completely removed.

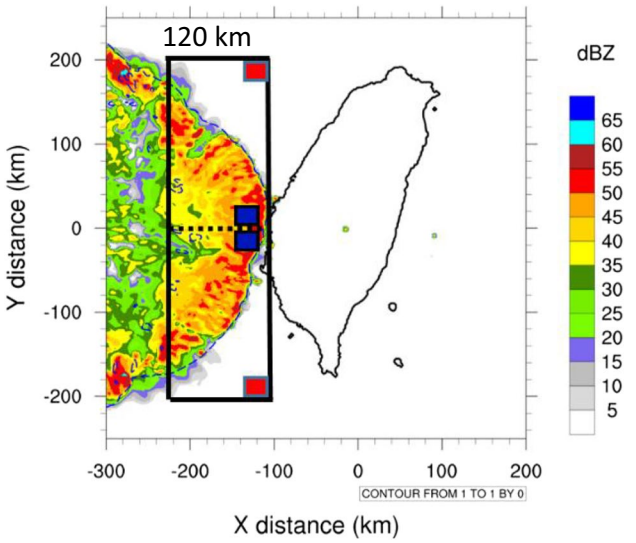

Fig. 6 Schematic diagram for calculating the spatial correlation coefficient (SCC). The center of bow echo ($y=0$) is regarded as the symmetry axis, and the blue boxes at north and south sides are the counterparts. Note that the red box (missing value) is ignored to avoid the overestimation of SCC

Table 1 Design of terrain-heights experiments

Experiment	Max terrain height (m)	Wind shear below 2.5 km (m s^{-1})	Max Froude number (F_{mt})	Reinitiate on the lee side
CTL	3312	10	0.43	N
TER56	2760	10	0.53	N
TER46	2208	10	0.67	N
TER36	1656	10	0.98	Y
TER26	1104	10	1.40	Y
TER16	552	10	2.90	Y
NTR	0	10	X	X

4 Model Results

4.1 Idealized Model Results: Control Experiment (CTL)

Figure 7 displays radar-reflectivity evolution of the idealized squall-line MCS for the control run. At the model time of 240 min, convection and precipitation on the lee side is evident (Fig. 7a). The lee-wave convection appears at the first 30 min and then develops into a convective line (not shown). Right after 240 min, a long warm thermal is inserted into the model to mimic a squall line; at 300 min, this long warm thermal evolves to its embryo stage (Fig. 7b). Notice that instead of inserting a warm bubble at the model initial time, we delay the insertion time until 240 min to prevent from the interference between lee-wave convection and the squall-line MCS represented by the warm bubble. Figure 7c shows that the idealized squall line has developed its mature stage before encountering the Taiwan terrain; meanwhile, the lee-wave precipitation has moved eastward away from Taiwan terrain by the westerly wind. In addition, the north–south

Table 2 Design of low-level wind-shear experiments

Experiment	Max terrain height (m)	Wind shear below 2.5 km (m s^{-1})	Max Froude number (F_{mt})	Reinitiate on the lee side
WS15.0	3312	15.0	0.46	Y
WS12.5	3312	12.5	0.45	N
CTL	3312	10.0	0.43	N
WS7.5	3312	7.5	0.39	N
WS5.0	3312	5.0	0.28	N

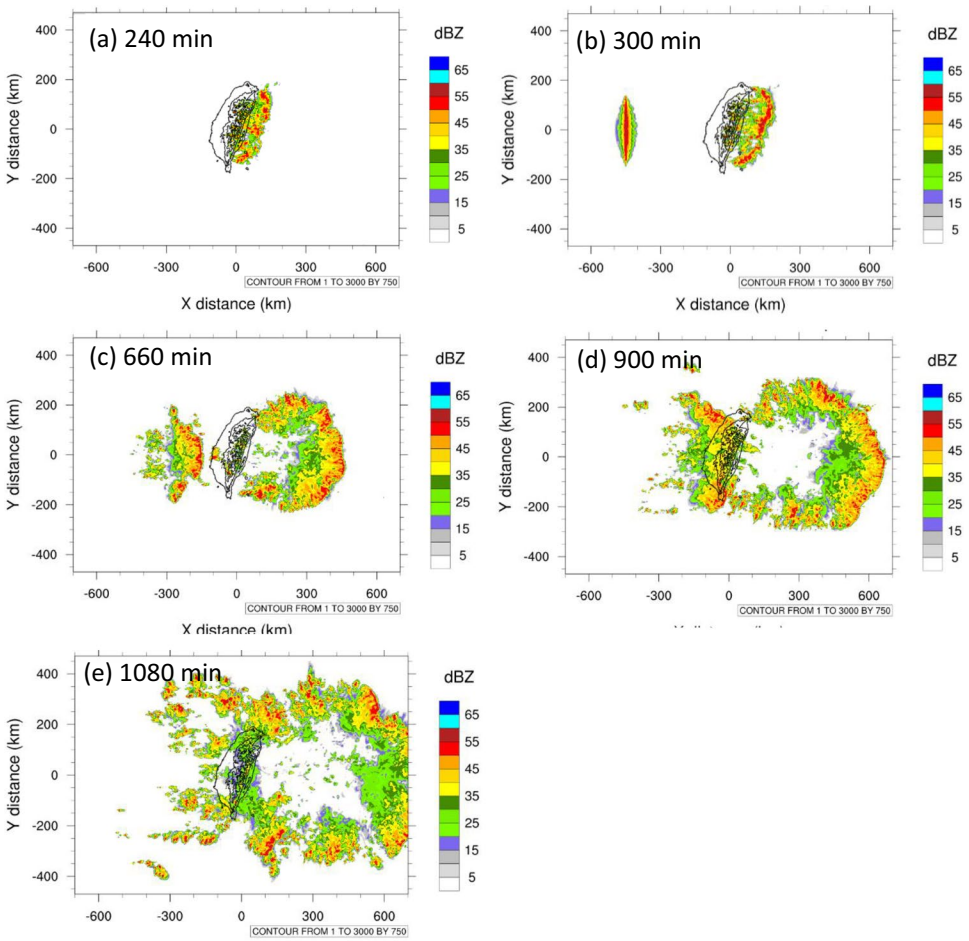

Fig. 7 Simulated radar CV plot of the full computational domain at **a** 240 min, **b** 300 min, **c** 660 min, **d** 900 min, and **e** 1080 min. Contour interval for terrain height is 750 m

length of precipitation area of the idealized squall line is approximately the same as the north–south length of Taiwan Island, similar to the case of the 19 April 2019 squall-line MCS (Fig. 1c). Later, the simulated squall line touches the Taiwan terrain and dissipates later over the lee side (Fig. 7d, e).

When we zoom in the region near Taiwan, the impacts of the terrain upon the squall line can be seen clearly, such as the upwind-side asymmetry and lee-side asymmetry as the observed radar CV shown in Fig. 1. Figure 8a displays that the radar reflectivity of the idealized squall-line MCS develops a symmetric bow-echo shape before encountering the terrain. The lee-wave precipitation moves away from Taiwan except for the northeast and southeast corners due to the convergence of the detouring winds (Kirshbaum and Schultz 2018). Figure 8b shows that the squall-line MCS precipitation pattern still remains nearly symmetric when the leading edge touches the terrain-height contour of 500 m. This is reasonable because the height over the western plain of Taiwan is not tall enough to block the movement of the squall line at this time; hence, the precipitation structure of the squall-line MCS does not alter significantly. The decisive transition occurs at later stage as shown in Fig. 8d. It is manifested that the leading line of the squall-line MCS evolves to an asymmetric structure with the southern leading line showing the north–south orientation but the northern leading line remaining the original northwest-southeast orientation. This simulation result resembles the precipitation pattern of the observed 19 April 2019 case (Fig. 1c). Furthermore, if we scrutinize the radar-echo intensity of the squall line, we find that the southern part also has stronger radar reflectivity as observed in the 19 April case. Eventually, Fig. 8e displays that the squall-line MCS dissipates on the lee side, and the leading edge of southern part moves faster than that of the northern part. This lee-side asymmetry is also similar to what we have found in the observation (Fig. 1e).

The vertical cross section in Fig. 9 is used to examine the evolution of the idealized squall-line MCS and the relation between the cold pool and terrain blocking effect. To make the vertical cross section more representative, this cross section is averaged within a 12-km strip along the *y* direction. Figure 9a illustrates the typical leading-convection region and trailing-stratiform region (with radar bright bands near the melting level at 4 km) as shown in the conceptual model of Houze et al. (1989; see their Fig. 1). A prominent cold

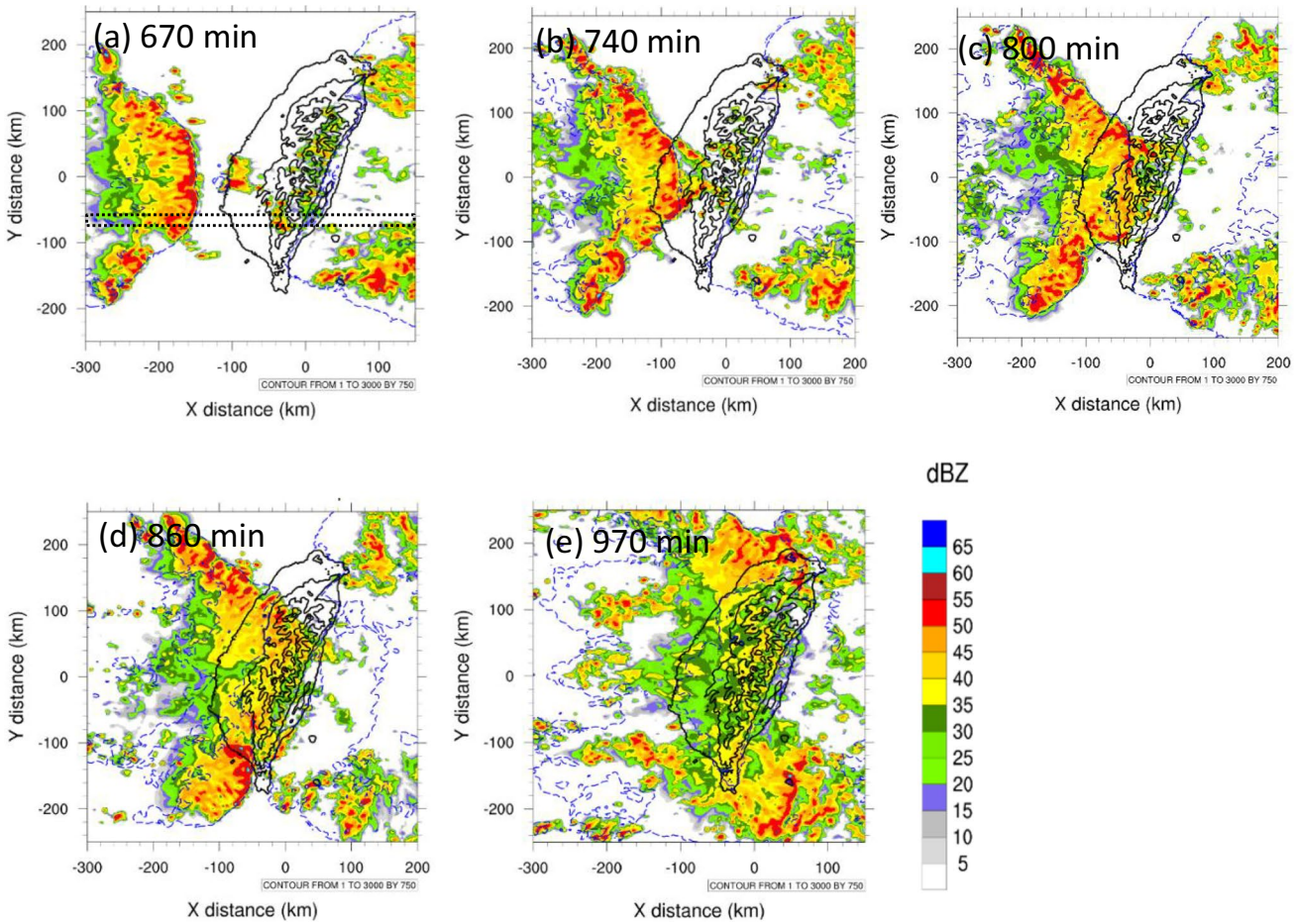

Fig. 8 Simulated radar CV plot near Taiwan at **a** 670 min, **b** 740 min, **c** 800 min, **d** 860 min, and **e** 970 min. Blue dotted line is the − 2 K contour for perturbation potential temperature, and the black dotted stripe area in (**a**) corresponds to the vertical cross section in Fig. 9

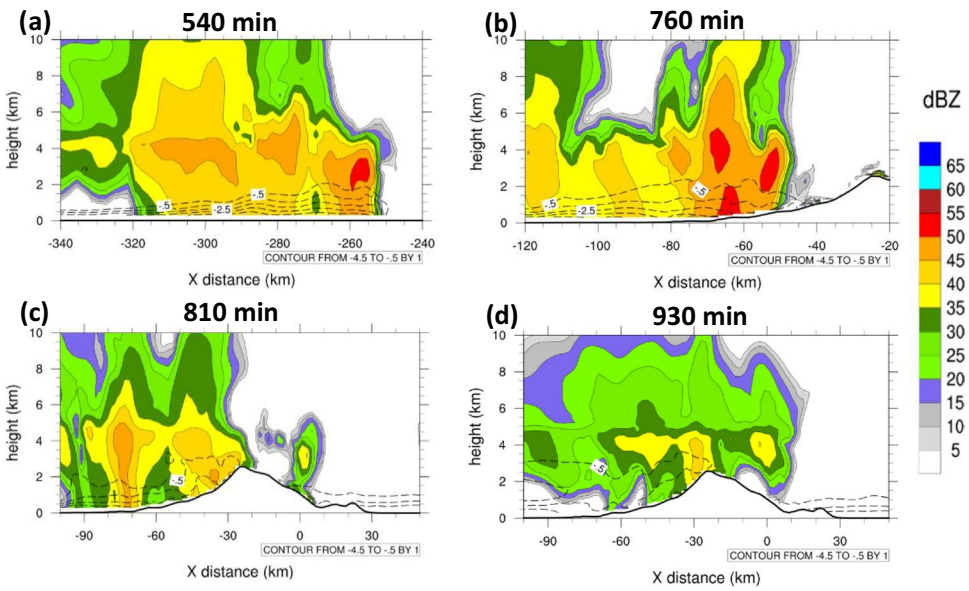

Fig. 9 Vertical cross sections of radar reflectivity (colored; in units of dBZ) and perturbation potential temperature (dotted line; contoured from − 0.5 K to − 4.5 K by 1 K): **a** 540 min, **b** 760 min, **c** 810 min, **d** 930 min. The horizontal position of the 12-km averaged vertical cross section is shown in Fig. 8a

pool (i.e. with negative potential-temperature perturbation) can be seen clearly below 2 km. Figure 9b displays that the leading-line convection is intensified over the up-wind slope because the terrain provides an extra mechanical lifting to enhance the upward motion at the leading edge (Teng et al. 2000; Frame and Markowski 2006). Figure 9c shows that the cold pool is mostly blocked by the terrain except for the − 0.5 K isotherm, and this blocking effect causes the cold pool to mainly spread around the terrain, instead of climbing over the hill. Consequently, the updraft at the leading edge is weakened by the downward motion on the lee side. The mountain-height Froude number (F_{mt}) is only 0.43, consistent with the fact that the cold pool is mainly blocked by terrain. Afterward, only stratiform precipitation region is remained (Fig. 9d). Notice that there is already cold air produced by the initial lee-wave precipitation (Fig. 7d) on the lee side before the arrival of the squall-line MCS (Fig. 9c, d). This pre-existing cold air also debilitates the ability of convection regeneration on the lee side (French and Parker 2014; Lombardo and Kading 2018).

4.2 Upwind-Side and Lee-Side Asymmetries of the Squall-Line MCS

After encountering Taiwan terrain, the southern (northern) leading line of the simulated squall-line MCS alters obviously (slightly) on the upwind side (Fig. 8). How does the Taiwan topography produce different structure changes over the northern and southern parts of the squall line? Figure 10a shows that the leading line of the simulated idealized squall line has a symmetric bow echo with the lowest-level wind perpendicular to the leading edge. Later, the cold pool encounters the 500-m terrain contour. Note that different terrain-ridge orientations of northern and southern Taiwan make the cold pool to detour in various manners (Fig. 10b). For the northern (southern) side, the terrain ridge orientation is mainly parallel (normal) to the wind direction. As a result, the northern leading line remains its original direction, and the surface wind accelerates (see northern box in Fig. 10b) possibly by the terrain channel effect (Skyllingstad et al. 2001; Hitzl et al. 2014). In contrast, the southern leading line changes the direction significantly due to the ridge orientation of the southern CMR (see southern box in Fig. 10b). The wind behind the southern leading edge is almost deflected by 90°, so the southern leading line changes its direction (Fig. 10c).

After the squall-line MCS moves to the lee side, the leading edge of southern part moves ahead of the northern part, because of the lee-side asymmetry (Fig. 10d). For the airflow in southern red box, it is hypothesize that the collision between the cold pool and the deflected wind reinforces the movement of the southern squall line (Fig. 8d and 10c). To verify this hypothesis, the convergence field is shown in Fig. 10e and f (before and after the landfall of the southern leading line on Taiwan). The wind convergence is indeed increased after landfall. Thus, it is confirmed that the wind deflection at southern part of the leading line leads to increased convergence, stronger vertical motion, and more intense convection for the squall-line MCS.

Figure 11 displays the 12-km averaged vertical cross section over Mount Snow. Firstly, when the squall-line MCS approaches the mountain, the upward motion is at the leading edge of the system (Fig. 11a, c). While the squall-line MCS climbs to the mountain top, the convection intensity decreases immediately due to the terrain blocking effect and no new convection is initiated on the lee side (Fig. 11b). Figure 11d shows that the potential temperature isotherms (isentropes) only ascend slightly on the downslope ($x \approx$ 20 km), indicating a weaker and insignificant hydraulic jump (Durran 1986, 1990). Figure 11f shows that the F_{cp} is below 1 (subcritical) on the upstream side (Fig. 11f) and at the peak (Fig. 11f), not a favorable condition for hydraulic jump to occur.

Figure 12 shows the 12-km averaged vertical cross section for southern Taiwan situation. When the squall line approaches the mountain (Fig. 12a), the upward motion also occur at the leading edge (Fig. 12c) as that in the northern part (Fig. 11c), but the scenario bifurcates later. Notice that the stronger downward motion on the steeper lee-side slope (slope ≈ 0.111) leads to an effective hydraulic jump with significant lifting of the isentrope near the surface (Fig. 12d). Figure 12e and f show that the F_{cp} within the cold pool is less than 1 (subcritical) in upstream area, but it becomes greater than 1 (supercritical) at the peak because of strong airflows above the peak. As a result, these factors (steeper downwind slope and occurring at surface) for the southern part favor convection initiation on lee side (Fig. 12b). Also notice the time is different between Figs. 8, 11 and 12, because the asymmetries and hydraulic jumps occur at various time.

4.3 Terrain-Heights Experiments

Terrain-height experiments include the no-terrain (NTR) to full-terrain (CTL) simulations, and the interval is one-sixth of actual terrain height (Table 1). Because the Froude number (F_{mt}) for the TER36 experiment is about 1 (0.98; see Table 1), for simplicity we separate the experiments into two groups: CTL-type and NTR-type groups.

Figure 13 shows the radar-reflectivity evolution of three terrain-height experiments. If Taiwan is completely removed (NTR), the squall-line MCS is almost symmetric for the entire period (Fig. 13g, h), although the symmetry slightly decreases at 930 min (Fig. 13i). For TER36 experiment, the convection is reinitiated on the lee side, and the bow-shaped leading edge is slightly affected by the terrain (Fig. 13f).

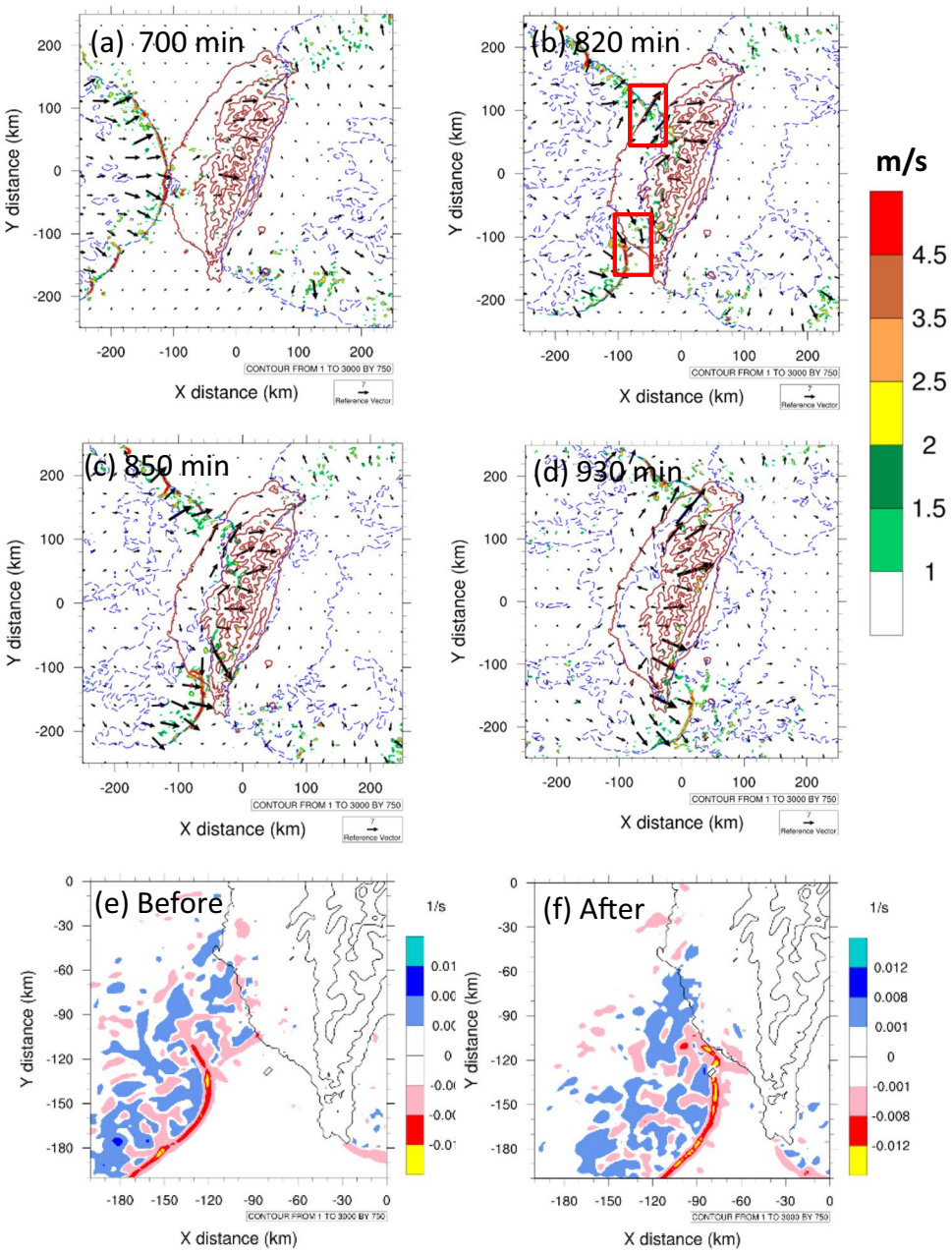

Fig. 10 The position between the cold-pool leading edge and Taiwan terrain at − 700 min, **b** 820 min, **c** 850 min, **d** 930 min. Blue dotted line is the perturbation potential temperature (contoured by − 2 K); black solid arrow is for the surface wind at the lowest model level (at 198 m). Taiwan terrain height is contoured at 1, 500, 1500, 2500, and 3000 m. Vertical velocity (in units of m s^{-1}) at 2-km height is colored in (**a**–**d**). The divergence field (colored; in units of s^{-1}) before and after squall-line's landing on southern Taiwan terrain is shown in (**e**) and (**f**), respectively

The TER36 experiment resembles the NTR experiment in the sense that the bow-shaped leading edge appears on the lee side, so we can categorize TER36 as the NTR-type group. The TER26 and TER16 experiments display similar structures as the TER36 experiment on the lee side, so we also classify them as the NTR-type group. We notice from Table 1 that the F_{mt} is greater than 1 when the terrain height is below or equal to that for TER36 (i.e., TER26 and TER16), and that the squall lines in these experiments have the ability to reinitiate convection on the lee side. However, if the terrain height is above that of TER36 (i.e., TER46, TER56, and CTL), the Froude number is less than 1, and no obvious convection is reinitiated on the lee side (Fig. 13c); hence, we can classify these experiments as the CTL-type group.

Figure 14 shows the propagation of the leading line of the simulated MCSs for three experiments. The structure is symmetric at the beginning (Fig. 14a, d, g), and the NTR experiment remains symmetric until 930 min (Fig. 14i). For TER36 experiment (Fig. 14f), its leading edge is not as continuous as that in NTR (Fig. 14i) owning to terrain effect. The TER36 experiment is supposed to have the ability to reinitiate new convection on the lee side, according to the Froude number ($F_{mt} \sim 1$), but it does not. It is because the cold air produced by lee-wave precipitation at the model initiation is accumulated on the lee side and inhibits convection

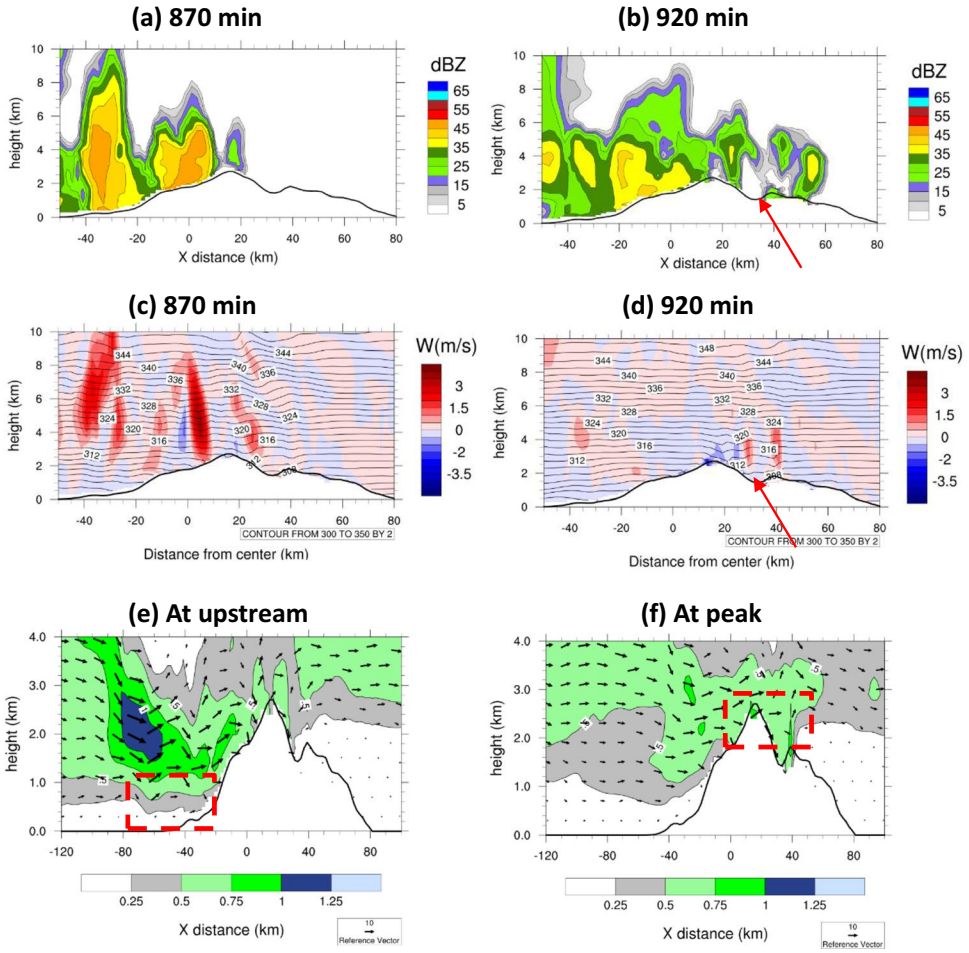

Fig. 11 Vertical cross sections of the radar reflectivity (colored) at **a** 870 min and **b** 920 min for northern Taiwan (Mount Snow); vertical cross sections of the vertical velocity (colored) and potential temperature (contoured by 2 K) at **c** 870 min and **d** 920 min for northern Taiwan (Mount Snow); vertical cross sections of the F_{cp} (colored) when the MCS system moves to **e** the upstream side and **f** mountain peak of the northern Taiwan (Mount Snow). The red arrows in **b** and **d** denote the locations of hydraulic jump. The dashed red boxes in **e** and **f** denote the leading-edge cold pool positions. The horizontal position of the 12-km averaged vertical cross section is shown in Fig. 3

re-initiation. As a result, the leading line of the TER36 is discontinuous.

Figure 15 shows the change of SCC at different stages. Four stages are chosen: Stage A is when the location of leading line is at west of Taiwan; Stage B is when the leading edge touches the 1-m height contour (border of Taiwan); Stage C is when the leading edge touches the 500-m height contour; Stage D is the most asymmetric stage on the upwind side. The SCC coefficient for NTR run is nearly 0.9 and slightly decreases to 0.86 at Stage D, as expected in the absence of Taiwan terrain. From Stage A to Stage B, the squall-line MCS is approaching the Taiwan border from the west, and all experiments have high SCCs. For Stage B to Stage C, the squall-line MCS starts to "feel" the impacts of Taiwan hills (below 500 m). Recall that the F_{mt} for TER36 experiment is near 1, so the terrain blocking effect is obvious for experiments with terrain heights equal to or above the peak of TER36 experiment. As a result, in this period, the SCC coefficient decreases for TER46 and TER56 experiments. In contrast, for experiments with peaks below the terrain height of TER36 experiment, the SCC coefficient either remains the same or increases slightly, because of the minor terrain blocking effect (TER26 and TER16 experiments). To some degree, TER36 experiment is like a flow-regime division to separate two different flow regimes when the squall-line MCS enters the hills area, and this is the reason why we show the change of SCCs for all terrain sensitivity experiments. From Stage C to Stage D, the SCCs for all experiments decrease significantly and the decreasing rate is approximately proportional to terrain height at stage D. This implies that the terrain peak height is a critical parameter for the squall-line symmetry, and higher terrain peak makes the squall-line MCS more asymmetric on the upwind side.

For the CTL experiment, it is not as symmetric as other experiments at first (Stage A), and the terrain might force the squall-line MCS to develop more asymmetric structures at the upslope stage (Teng et al. 2000). The increasing SCC (from Stage B to Stage C) does not match the regime for the low Froude number, but it is acceptable because the degree of symmetry for the CTL at first is too low as comparing with other experiments. Later, the SCC coefficient of the CTL drops significantly from Stage C to Stage D due to the steep terrain. Notice that radar observation of the squall-line MCS on 19 April 2019 has similar evolution of SCC from

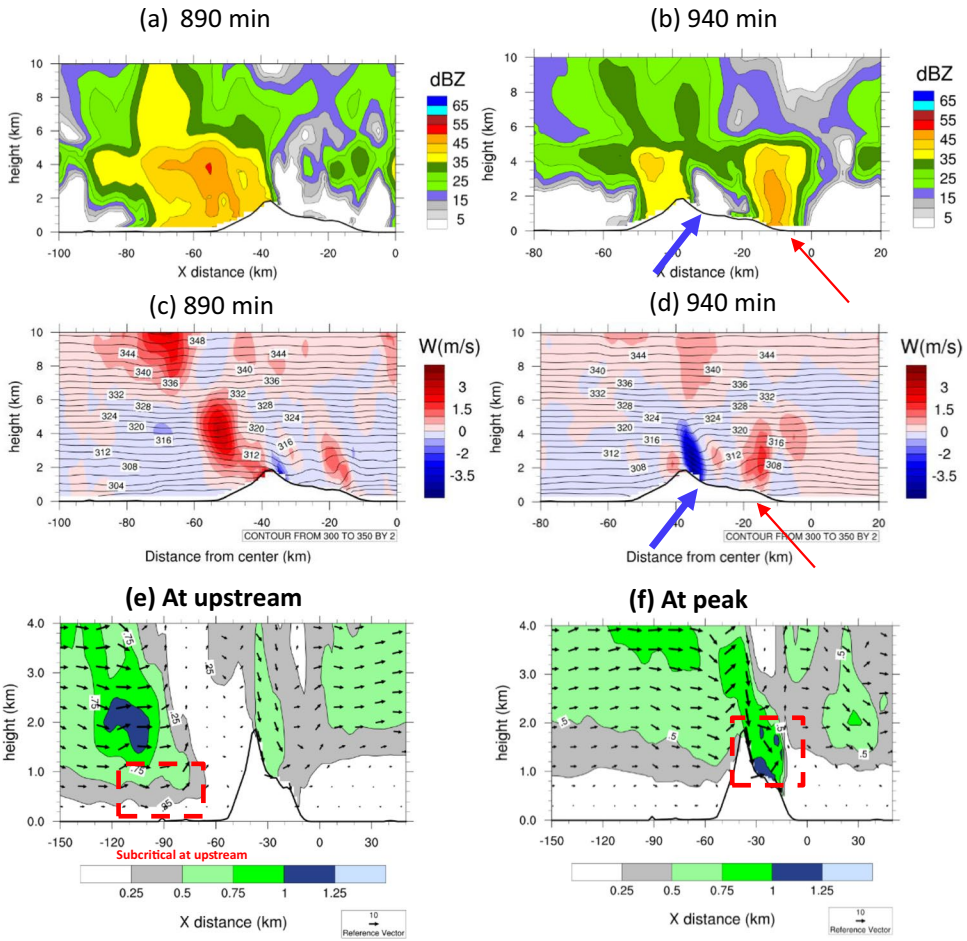

Fig. 12 **a, b** As in Fig. 11a, b, but for the southern Taiwan (Southern CMR) at 890 min and 940 min; **c, d** as in Fig. 11c, d, but for the southern Taiwan (Southern CMR) at 890 min and 940 min; **e, f** as in Fig. 11e, f, but for the southern Taiwan when the squall-line MCS system is at the upstream side and mountain peak. The red arrows in **b, d** denote the locations of hydraulic jump, and the blue arrows indicate the locations of strong downward motion. The horizontal position of the 12-km averaged vertical cross section is shown in Fig. 3

Stage B to Stage D as the CTL, as expected from the fact that the observed squall line experienced the same full degree of terrain effect as the CTL simulation.

4.4 Low-Level Wind-Shear Experiments

In these experiments, we change the wind speed systematically in order to examine its influence on the F_{mt} and squall-line MCS evolution (Table 2 and Fig. 2c). We may use the RKW theory (Rotunno et al. 1988) to examine the results. The RKW theory, which considers the balance between horizontal vorticity created by the cold pool and the vorticity by environmental low-level wind shear, can be used to explain different evolution of the squall line before the influence of Taiwan terrain (Fig. 16a, d, g). The leading-line convection remains upright when the vorticity by wind shear is strong enough to balance with that by the cold pool (WS15.0; Fig. 16a). On the other hand, the leading-line convection becomes up-shear tilted and trailing stratiform precipitation is evident when the vertical shear is weak and the cold pool dominates (WS5.0; Fig. 16g). Large variations in precipitation occur among the experiment when the simulated squall lines are on the upwind side of Taiwan terrain (Fig. 16b, e, h). The fact that the WS15.0 experiment can initiate new convection on the lee side with low F_{mt} (Fig. 16c and Table 2) is not consistent with the results in previous section that for small Froude number, and it is because the strong hydraulic jumps produced by strong mid- and upper-level winds (to be shown in Fig. 17a, c).

Figure 17a and b show that the new convection exists on the lee side in WS15.0 experiment but not in CTL experiment, and that the hydraulic jump effect for the WS15.0 experiment is significantly stronger than that for the CTL run. The reason is the intensity of mid- and upper-level winds. The wind below 1 km does not change significantly among different shear experiments (Table 2 and Fig. 2c), so the Froude number (F_{mt}) is still small even we increase the low-level shear. However, the environmental wind between 2.5- and 5.0-km heights offers an extra dynamical force to help the flow to have a transition from subcritical ($F_{cp} < 1$) at upstream to supercritical ($F_{cp} > 1$) at mountain peak (Durran 1986, 1990), which induces hydraulic jump on the lee side (Fig. 17g). But the flow transition does not occur in the CTL experiment; as a result, no obvious hydraulic jump is found (Fig. 17h). Therefore, only using mountain-height Froude number (F_{mt}) to decide whether the convection will

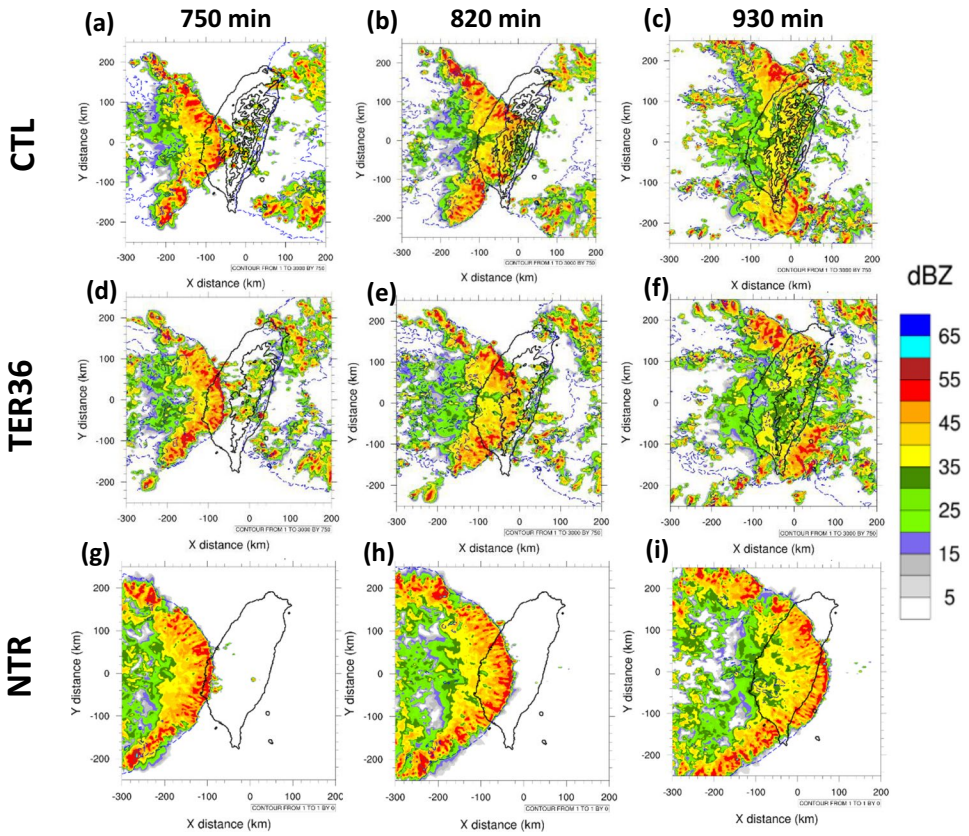

Fig. 13 As in Fig. 7, but for the terrain experiments. Upper row is for CTL, middle row is for TER36, and lower row is for NTR experiment. Left column of panel **a**, **d**, **g** is for simulation time at 750 min; middle column of panel **b**, **e**, **h** is for simulation time at 820 min; right column of panel **c**, **f**, **i** is for simulation time at 930 min

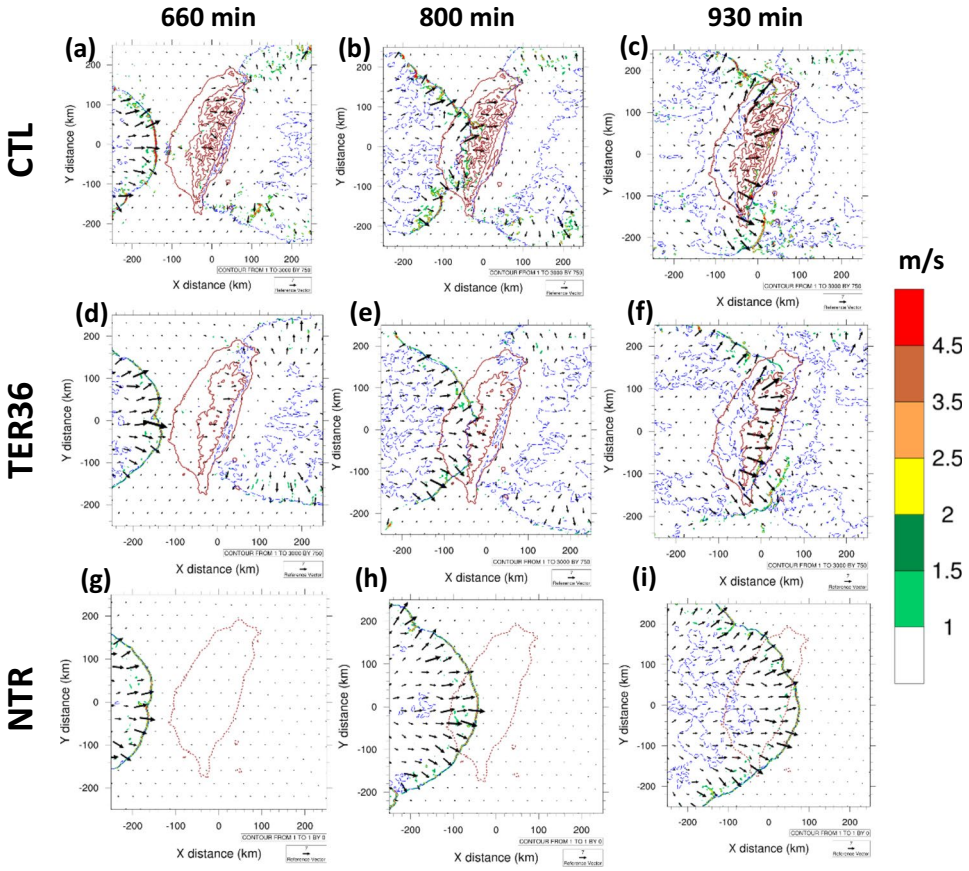

Fig. 14 As in Fig. 10, but for the terrain experiments. Upper row is for CTL, middle row is for TER36, and lower row is for NTR experiments. Left column of panel **a**, **d**, **g** is for simulation time at 660 min; middle column of panel **b**, **e**, **h** is for simulation time at 800 min; right column of panel **c**, **f**, **i** is for simulation time at 930 min

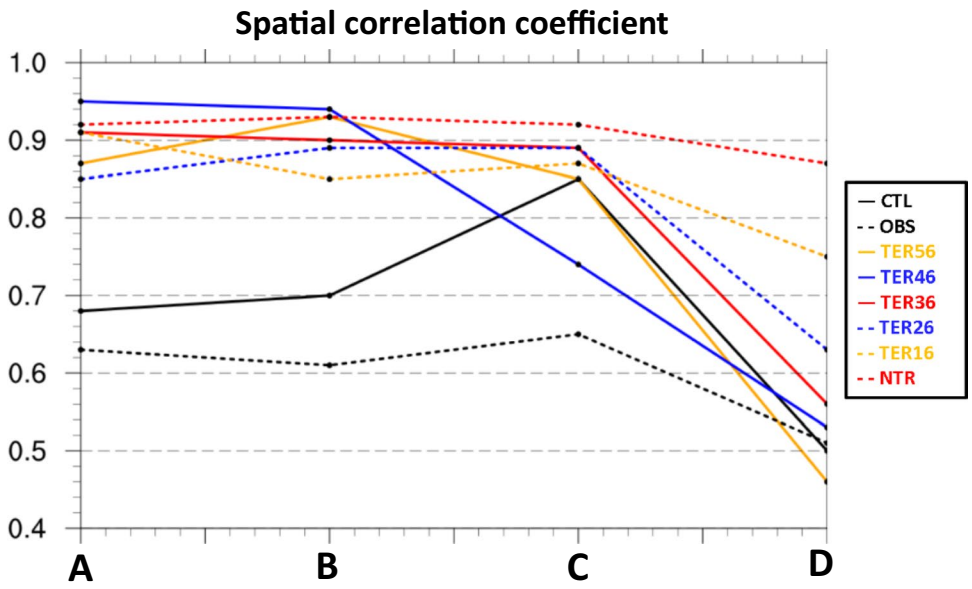

Fig. 15 The spatial correlation coefficient (SCC) of the squall-line MCS structures at four stages for the observation (OBS; black dotted), CTL (black solid), TER56 (orange solid), TER46 (blue solid), TER36 (red solid), TER26 (blue dotted), TER16 (orange dotted), and NTR (red dotted) experiments. Definitions for Stage A, B, C, and D are described in the text

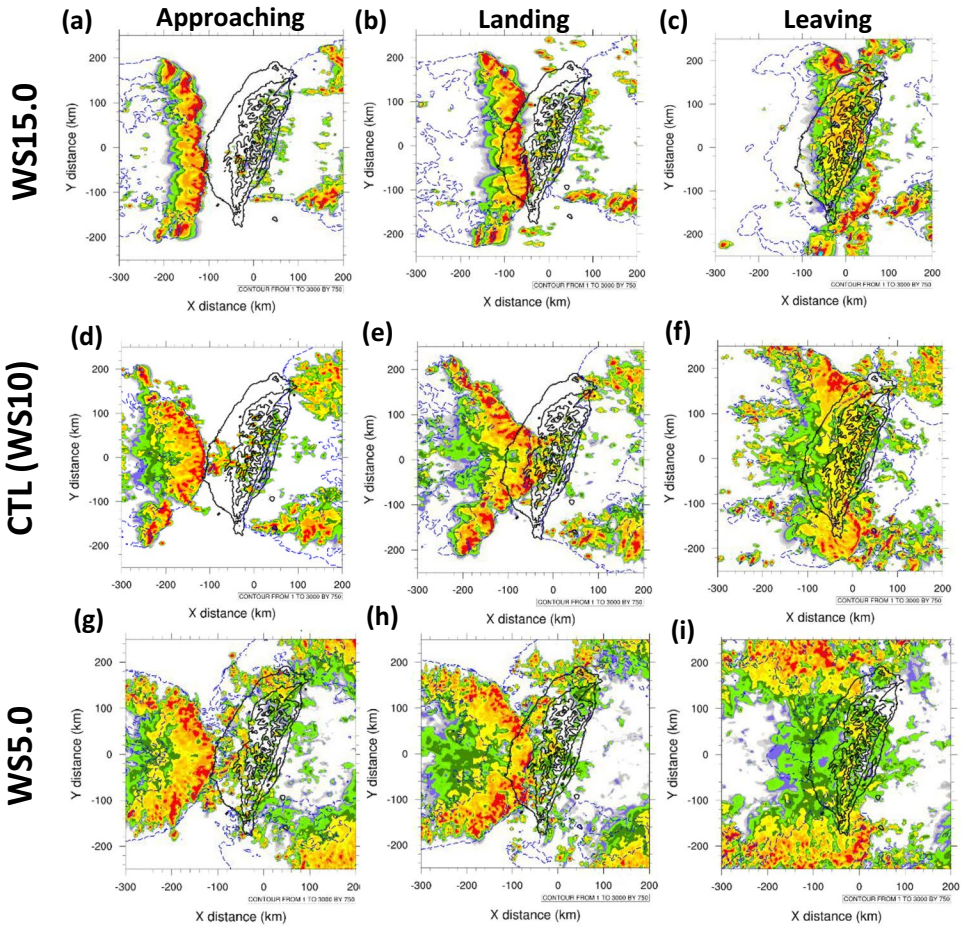

Fig. 16 As in Fig. 13, but for the low-level wind shear experiments. Different timings are chosen when the squall-line MCS is approaching (left column), landing (middle column), and leaving (right column) the Taiwan mountain

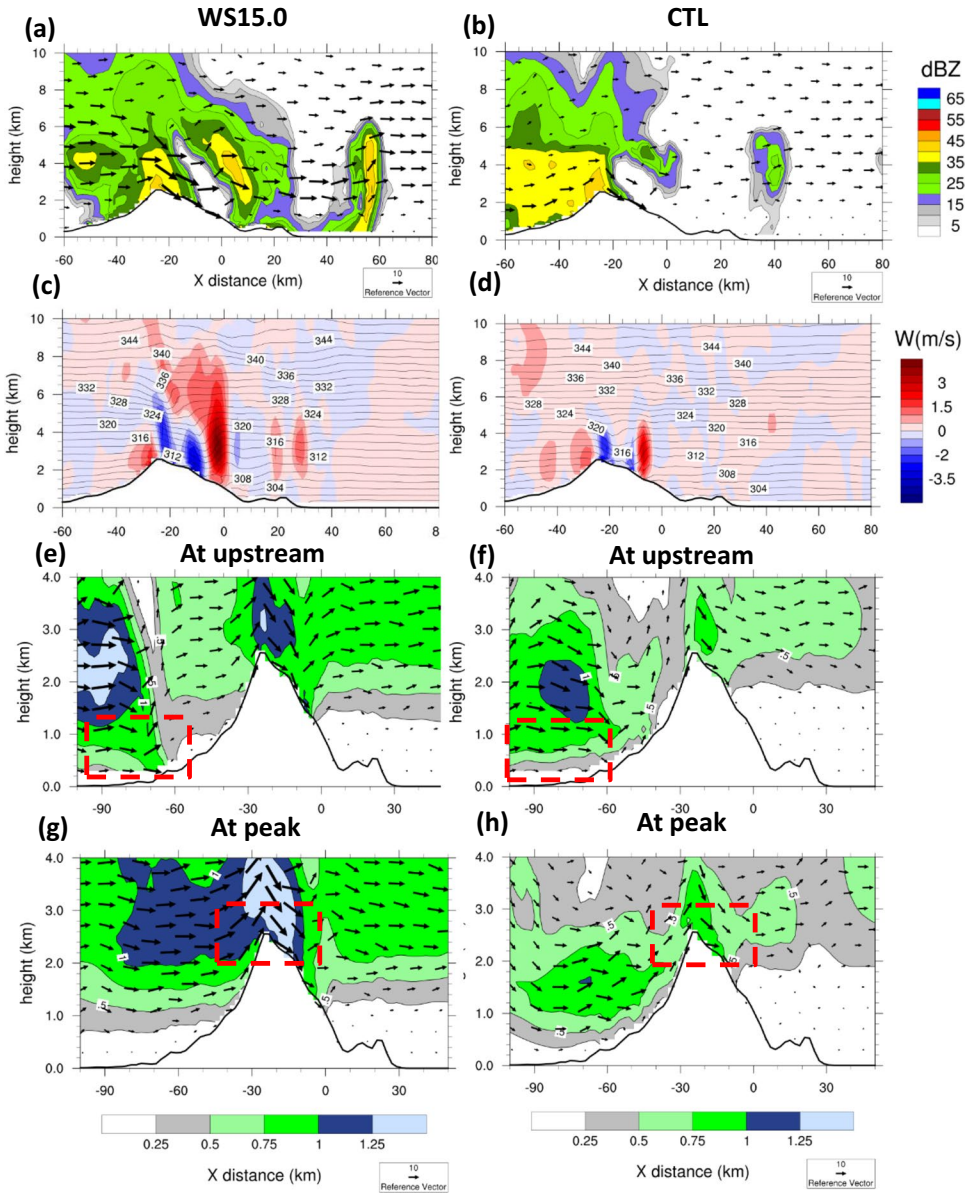

Fig. 17 Vertical cross sections of **a** the radar reflectivity (colored) and along-plane vectors, **c** the vertical velocity (colored) and potential temperature (contoured by 2 K), **e** the Froude number (colord; F_{cp}) when the squall-line MCS is at the upstream side, and **g** the Froude number (colored; F_{cp}) when the squall-line MCS system is at the mountain peak of the southern CMR for the WS15.0 experiment. Panels **b**, **d**, **f**, **h** are similar to panels **a**, **c**, **e**, **g** but for the CTL experiment. The dashed red boxes in **g** and **h** denote the leading-edge cold pool positions

be reinitiated on the lee side, where there is significant vertical wind shear, may not be appropriate.

4.5 Schematic Diagrams for Upwind-Side and Lee-Side Asymmetries

Figure 18 is the schematic diagram for the evolution of upwind-side asymmetry. Firstly, the squall-line MCS develops its mature stage with the bow-shaped leading line (Step 1), remaining its symmetric structure before the encounter with Taiwan terrain. The surface wind is nearly perpendicular to the leading line (Step 2). If we focus on the ridge orientation, the northern terrain (Mount Snow) is mainly in northeast-southwest orientation, approximately parallel to the wind direction behind the leading edge. On the contrary, the southern terrain (southern CMR) is in north–south orientation, nearly normal to the wind direction behind the leading line. The south side of the northern leading line accelerates because the wind is parallel to the ridge orientation. As a result, the leading line rotates counterclockwise (Step 3). But for the southern side, the central part of squall line decelerates because the wind behind the leading line is nearly normal to the terrain (Step 4). The different propagation speed between different parts of the leading line leads to the asymmetry on the upwind side. Finally, Step 5 indicates that the convection ahead of the southern squall line intensifies owing to the surface-wind convergence and cold-pool collision.

Figure 19 is the schematic diagram for the lee-side asymmetry in two vertical cross sections. For Mount Snow, the horizontal width of the mountain is extensive

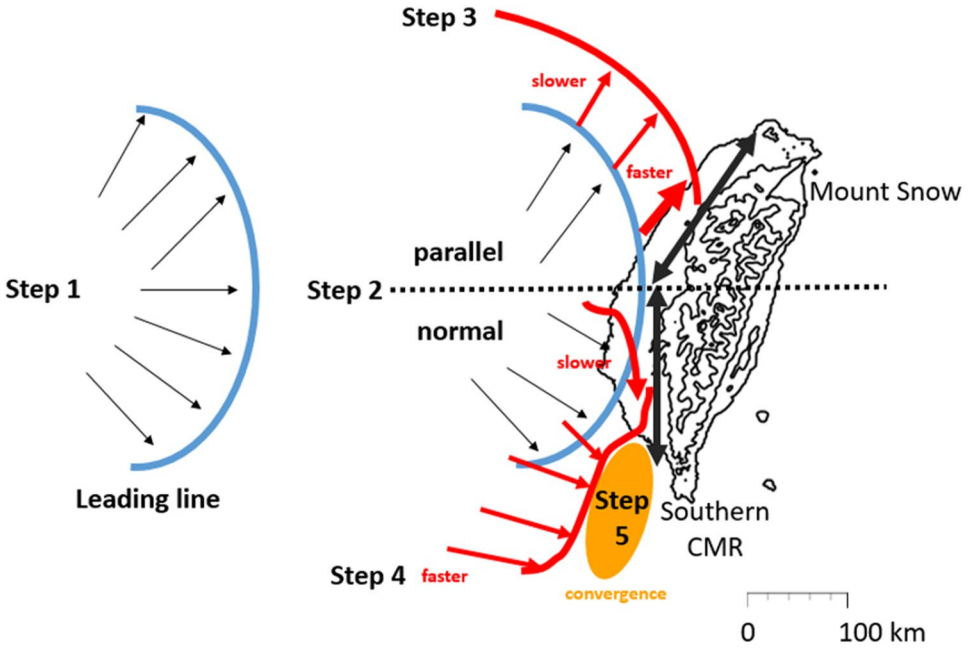

Fig. 18 Schematic diagram for the five evolution steps for the upwind-side asymmetry of squall-line MCS. Five steps are explained in the text. Orange area is the convergence area. Black solid arrows near Taiwan denote the ridge orientation of Taiwan mountain range. The black dotted line separates the squall-line MCS into the northern and southern parts

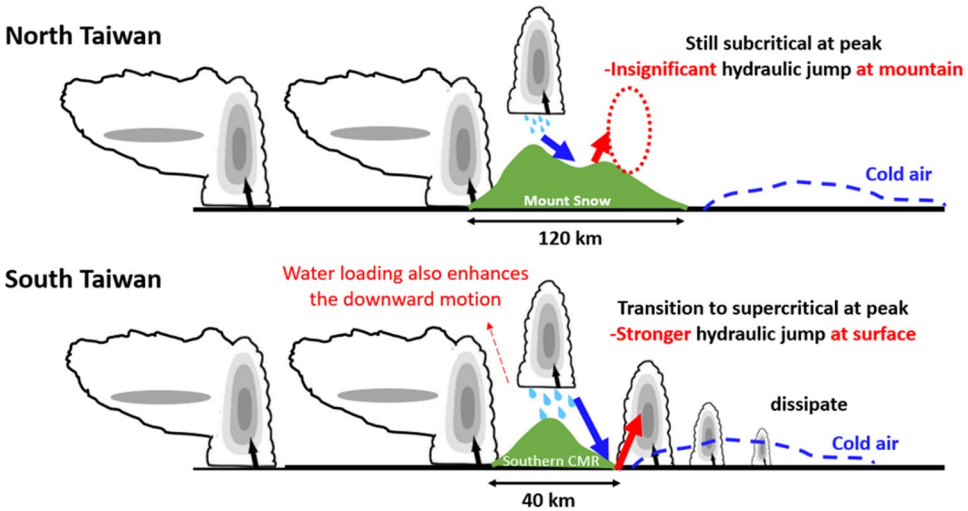

Fig. 19 Schematic diagram for the leeside asymmetry of the squall line at **a** the northern (Mount Snow) and **b** southern Taiwan (Southern CMR). The cloud outline is shown, gray shading indicates the radar reflectivity convective cores and the bright band in the stratiform region. Blue arrow represents the downward motion, red arrow is for hydraulic jump, and blue dotted line displays the cold air produced by the gravity-wave convection and precipitation

(120 km), and the lee slope is moderate (0.067); the flow-regime transition from subcritical at upstream to supercritical at mountain peak does not occur and the lee-side subsidence is not strong at peak. The weak hydraulic jump occurs over mountainous area, which would not favor convection re-initiation (Fig. 19a). However, the situation is different over the southern CMR. The horizontal width (40 km) is only a third of that for Mount Snow, and the slope on the lee-wind side is steeper (0.111); the crucial flow-regime transition does occur and the subsidence is stronger on the lee side. Furthermore, the hydraulic jump occurs at near the surface. All these factors support the convection re-initiation on the lee side over southern CMR (Fig. 19b).

5 Conclusions

A mature squall-line MCS developed a bow-echo shape and approached Taiwan from the west on 19 April 2019, causing fierce gust wind up to 20 m s^{-1} and heavy rainfall with hailstones over several places in Taiwan. After the contact with Taiwan terrain, the originally symmetric structure of this squall line altered with significant upwind-side and lee-side asymmetries, which are the main scientific foci of this study. The idealized WRF simulations with horizontal grid size of 2 km (in the absence of the effects of Coriolis force, radiation and horizontal heterogeneity) were conducted in order to systematically

examine the relationships among the Froude numbers (F_{mt} and F_{cp}), squall-line structure, and hydraulic jump.

Idealized simulations show that the squall-line MCS develops its bow-echo shape with nearly symmetric structure before the arrival on Taiwan, similar to the observed case on 19 April 2019. According to the mountain-height Froude number (F_{mt}), the low-level air at the leading edge of the squall-line MCS is blocked by the steep Taiwan terrain; as a result, the wind deflection is apparent. Different ridge orientations between northern (northeast-southwest) and southern (north–south) Taiwan terrain bring about the upwind-side asymmetry (Fig. 18). On the other hand, the different mountain width, downwind slope, and the transition of the flow regime (i.e., hydraulic jump) from subcritical at upstream to supercritical at mountain peak lead to the lee-side asymmetry. Also, the intensity and location of the hydraulic jumps depend on the width and downwind slope of mountain. To be specific, the southern (northern) terrain is narrower (wider) and the downwind slope is steeper (more moderate). In addition, the southern CMR (Mount Snow) has (lacks of) the flow transition from subcritical at upstream to supercritical at peak, causing significant (weak) hydraulic jump which occurs over surface (mountainous area) and the convection can (cannot) be reinitiated on the lee side (Fig. 19).

Terrain-height experiments were performed to investigate the terrain blocking effect. The TER36 experiment separates these experiments into two groups. One is that the squall-line structure becomes more symmetric after the squall-line's arrival on lower terrain, and the other is that the squall line becomes asymmetric. It depends on whether the mountain-height Froude number (F_{mt}) ≥ 1 (TER36, TER26 and TER16 experiments) or not (TER46 and TER56 experiments). The terrain blocking effect is the main reason for the asymmetric structure of the squall-line MCS after its arrival on the steep Taiwan terrain.

Low-level wind shear experiments are also conducted to investigate the asymmetry and hydraulic jump on the lee side. In low-level shear experiments, we find that the mid- to high-level winds are also important for the hydraulic jump, because it offers an extra dynamic forcing to support flow-regime transition at peak.

In summary, the idealized WRF simulations in this study provide us an opportunity to clarify and explore the effects of Taiwan terrain on a squall-line MCS. Nevertheless, the squall line on 19 April 2019, which is an eastward moving squall-line MCS, is not a frequent case during the Mei-Yu season. Other progression directions of the squall-line system are more common, such as southeastward or northeastward directions. For future studies, different impinging angles between the leading line of the squall-line MCS and mountain ridge orientations of Taiwan should be performed to examine whether the terrain-blocking hypothesis and hydraulic-jump effects obtained in this study can be applied to other scenarios. Finally, more studies of the squall-line MCSs impinging on high mountains over other geographic regions should be conducted to verify the results obtained from this study near Taiwan.

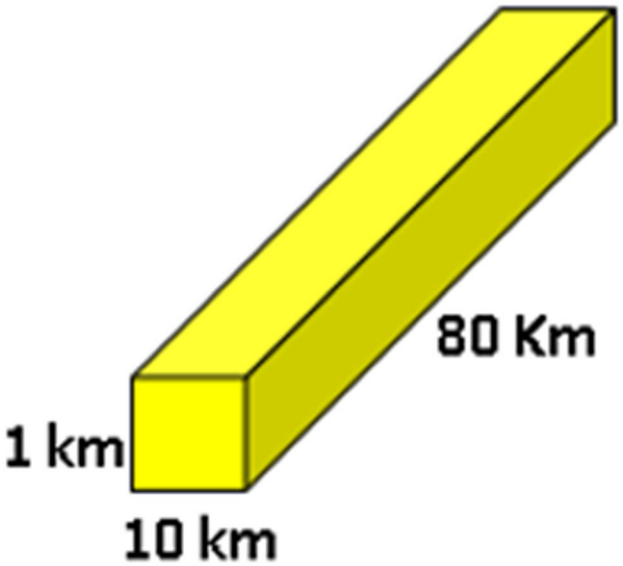

Fig. 20 The atmospheric volume in the calculation of Froude number F_{mt}

Appendix: Details for calculating the Froude Numbers of F_{mt} and F_{cp}

We describe the procedures in calculating the Froude numbers (F_{mt} and F_{cp}) in this Appendix, in additional to the graphic illustration given in Fig. 5. For Froude number F_{mt}, its definition is given in Eq. (1), where the variables U_{avg} and N_{avg} are averaged for the same atmospheric volume (shown in Fig. 20) at the leading edge of squall line (with a zonal width of 10 km, a meridional length of 80 km for $y = -40$ km ~ $+40$ km, and a depth of 1 km for $z = 0 \sim 1$ km) in a Lagrangian framework, and H_{mt} is the highest mountain peak in the range of $y = -40$ km ~ $+40$ km. For Froude number F_{cp}, its definition is given in Eq. (3), where the variables U and N are the values at grid points, and the cold-pool depth is the depth of cold-air perturbation (as defined by the depth of the contour of $\theta' = -1.5$ K), which approximately remained constant at $z = 1.5$ km (i.e., $H_{cp} = 1.5$ km) before the cold pool encountered Taiwan terrain.

Acknowledgements Constructive comments by two reviewers on our manuscript are highly appreciated. We thank the Central Weather Bureau in Taiwan for providing the observation data. Parts of the results were from the first author's M.S. thesis study at National Taiwan University. This work was supported by the Ministry of Science

and Technology in Taiwan under Grants MOST 108-2625-M-052-003, MOST 108-2111-M-002-011-MY2, and MOST 110-2111-M-002-014.

References

Armi, L., Mayr, G.J.: The descending stratified flow and internal hydraulic jump in the lee of the sierras. J. Appl. Meteorol. Climatol. **50**, 1995–2011 (2011)

Chu, C., Lin, Y.: Effects of orography on the generation and propagation of mesoscale convective systems in a two-dimensional conditionally unstable Flow. J. Atmos. Sci. **57**, 3817–3837 (2000)

Chen, S., Lin, Y.: Effects of moist Froude number and CAPE on a conditionally unstable flow over a mesoscale mountain ridge. J. Atmos. Sci. **62**, 331–350 (2005)

Durran, D.R.: Another look at downslope windstorms. Part I: the development of analogs to supercritical flow in an infinitely deep, continuously stratified fluid. J. Atmos. Sci. **43**, 2527–2543 (1986)

Durran, D.R.: Mountain waves and downslope winds. In: Blumen, W. (ed.) Atmospheric Processes over Complex Terrain. Meteorological Monographs, vol. 23, pp. 59–81. American Meteorological Society, Boston (1990)

Fang, Z.: The preliminary study of medium-scale cloud cluster over Changjiang basin in summer. Adv. Atmos. Sci. **2**, 334–340 (1985)

French, A.J., Parker, M.D.: Numerical simulations of bow echo formation following a squall line–supercell merger. Mon. Wea. Rev. **142**, 4791–4822 (2014)

Frame, J., Markowski, P.: The interaction of simulated squall lines with idealized mountain ridges. Mon. Wea. Rev. **134**, 1919–1941 (2006)

Fovell, R.G., Tan, P.: The temporal behavior of numerically simulated multicell-type storms. Part II: the convective cell life cycle and cell regeneration. Mon. Wea. Rev. **126**, 551–577 (1998)

Hitzl, D.E., Chen, Y., Van Nguyen, H.: Numerical simulations and observations of airflow through the 'Alenuihāhā' channel, Hawaii. Mon. Wea. Rev. **142**, 4696–4718 (2014)

Hong, S., Pan, H.: Nonlocal boundary layer vertical diffusion in a medium-range forecast model. Mon. Wea. Rev. **124**, 2322–2339 (1996)

Houze, R.A., Rutledge, S.A., Biggerstaff, M.I., Smull, B.F.: Interpretation of Doppler weather radar displays of midlatitude mesoscale convective systems. Bull. Am. Meteor. Soc. **70**, 608–619 (1989)

Jou, B.J.-D., Lee, W.C., Johnson, R.H.: An overview of SoWMEX/TiMREX. In: Chang, C.P. (ed.) The Global Monsoon System: Research and Forecast. World Scientific Series on Asia-Pacific Weather and Climate, vol. 5, pp. 303–318. World Scientific Publishing, Singapore (2011)

Karyampudi, V.M., Koch, S.E., Chen, C., Rottman, J.W., Kaplan, M.L.: The influence of the Rocky mountains on the 13–14 April 1986 severe weather outbreak. Part II: evolution of a prefrontal bore and its role in triggering a squall line. Mon. Wea. Rev. **123**, 1423–1446 (1995)

Kirshbaum, D.J., Schultz, D.M.: convective cloud bands downwind of mesoscale mountain ridges. J. Atmos. Sci. **75**, 4265–4286 (2018)

Kuo, Y.-H., Chen, G.T.-J.: The Taiwan area mesoscale experiment: an overview. Bull. Am. Meteorol. Soc. **71**, 488–503 (1990)

Letkewicz, C.E., Parker, M.D.: Impact of environmental variations on simulated squall lines interacting with terrain. Mon. Wea. Rev. **139**, 3163–3183 (2011)

Lim, K.-S.S., Hong, S.-Y.: Development of an effective double-moment cloud microphysics scheme with prognostic cloud condensation nuclei (CCN) for weather and climate models. Mon. Wea. Rev. **138**, 1587–1612 (2010)

Lin, Y., Joyce, L.E.: A further study of the mechanisms of cell regeneration, propagation, and development within two-dimensional multicell storms. J. Atmos. Sci. **58**, 2957–2988 (2001)

Lin, Y.-L., Deal, R.L., Kulie, M.S.: Mechanisms of cell regeneration, development, and propagation within a two-dimensional multicell storm. J. Atmos. Sci. **55**, 1867–1886 (1998)

Lombardo, K., Kading, T.: The behavior of squall lines in horizontally heterogeneous coastal environments. J. Atmos. Sci. **75**, 1243–1269 (2018)

Long, R.R.: A laboratory model resembling the "Bishop-wave" phenomenon. Bull Am. Meteorol. Soc. **34**, 20–211 (1953)

Miglietta, M.M., Rotunno, R.: Numerical simulations of conditionally unstable flows over a mountain ridge. J. Atmos. Sci. **66**, 1865–1885 (2009)

Ninomiya, K., Akiyama, T., Ikawa, M.: Evolution and fine structure of a long-lived meso-α-scale convective system in a Baiu front zone. Part I: evolution and meso-β-scale characteristics. J. Meteorol. Soc. Jpn. **66**, 331–350 (1988)

Reeves, H.D., Lin, Y.: The effects of a mountain on the propagation of a preexisting convective system for blocked and unblocked flow regimes. J. Atmos. Sci. **64**, 2401–2421 (2007)

Rotunno, R., Klemp, J.B., Weisman, M.L.: A theory for strong, long-lived squall lines. J. Atmos. Sci. **45**, 463–485 (1988)

Skamarock, W.C., Klemp, J.B., Dudhia, J., Gill, D.O., Barker, D.M., Duda, M.G., Huang, X.-Y., Wang, W., Powers, J.G.: A description of the advanced research WRF version 3. NCAR Tech. Note NCAR/ TN-4751STR (2008)

Skyllingstad, E.D., Barbour, P., Dorman, C.E.: The dynamics of northwest summer winds over the Santa Barbara channel. Mon. Wea. Rev. **129**, 1042–1061 (2001)

Tai, S., Liou, Y., Sun, J., Chang, S.: The development of a terrain-resolving scheme for the forward model and its adjoint in the four-dimensional variational Doppler radar analysis system (VDRAS). Mon. Wea. Rev. **145**, 289–306 (2017)

Teng, J.-H., Chen, C.-S., Wang, T.-C.C., Chen, Y.-L.: Orographic effects on a squall line system over Taiwan. Mon. Wea. Rev. **128**, 1123–1138 (2000)

Weisman, M.L.: The genesis of severe, long-lived bow echoes. J. Atmos. Sci. **50**, 645–670 (1993)

Weisman, M.L., Rotunno, R.: "A theory for strong long-lived squall lines" revisited. J. Atmos. Sci. **61**, 361–382 (2004)

Weisman, M.L., Skamarock, W.C., Klemp, J.B.: The resolution dependence of explicitly modeled convective systems. Mon. Wea. Rev. **125**, 527–548 (1997)

Yang, M.-J., Houze, R.A., Jr.: Multicell squall line structure as a manifestation of vertically trapped gravity waves. Mon. Wea. Rev. **123**, 641–661 (1995a)

Yang, M.-J., Houze, R.A., Jr.: Sensitivity of squall-line rear inflow to ice microphysics and environmental humidity. Mon. Wea. Rev. **123**, 3175–3193 (1995b)